



Modulation of Sialic Acid Dependence Influences the Central Nervous System Transduction Profile of Adeno-associated Viruses

Blake H. Albright,^{a,b} Katherine E. Simon,^c Minakshi Pillai,^b Garth W. Devlin,^c Aravind Asokan^{c,d}

^aCurriculum in Genetics and Molecular Biology, University of North Carolina at Chapel Hill, Chapel Hill, North Carolina, USA

^bGene Therapy Center, University of North Carolina at Chapel Hill, Chapel Hill, North Carolina, USA

^cDepartment of Surgery, Duke University School of Medicine, Durham, North Carolina, USA

^dDepartment of Molecular Genetics and Microbiology, Duke University School of Medicine, Durham, North Carolina, USA

ABSTRACT Central nervous system (CNS) transduction by systemically administered recombinant adeno-associated viral (AAV) vectors requires crossing the blood-brain barrier (BBB). We recently mapped a structural footprint on the AAVrh.10 capsid, which, when grafted onto the AAV1 capsid (AAV1RX), enables viral transport across the BBB; however, the underlying mechanisms remain unknown. Here, we establish through structural modeling that this footprint overlaps in part the sialic acid (SIA) footprint on AAV1. We hypothesized that altered SIA-capsid interactions may influence the ability of AAV1RX to transduce the CNS. Using AAV1 variants with altered SIA footprints, we map functional attributes of these capsids to their relative SIA dependence. Specifically, capsids with ablated SIA binding can penetrate and transduce the CNS with low to moderate efficiency. In contrast, AAV1 shows strong SIA dependency and does not transduce the CNS after systemic administration and, instead, transduces the vasculature and the liver. The AAV1RX variant, which shows an intermediate SIA binding phenotype, effectively enters the brain parenchyma and transduces neurons at levels comparable to the level of AAVrh.10. In corollary, the reciprocal swap of the AAV1RX footprint onto AAVrh.10 (AAVRX1) attenuated CNS transduction relative to that of AAVrh.10. We conclude that the composition of residues within the capsid variable region 1 (VR1) of AAV1 and AAVrh.10 profoundly influences tropism, with altered SIA interactions playing a partial role in this phenotype. Further, we postulate a Goldilocks model, wherein optimal glycan interactions can influence the CNS transduction profile of AAV capsids.

IMPORTANCE Understanding how viruses cross the blood-brain barrier can provide insight into new approaches to block infection by pathogens or the ability to exploit these pathways for designing new recombinant viral vectors for gene therapy. In this regard, modulation of virus-carbohydrate interactions by mutating the virion shell can influence the ability of recombinant viruses to cross the vascular barrier, enter the brain, and enable efficient gene transfer to neurons.

KEYWORDS AAV, brain, carbohydrate, cell surface receptor, gene therapy, neurotropism, sialic acid, virus-host interactions

Adeno-associated viral (AAV) vectors for gene therapy applications are being clinically evaluated for a range of genetic disorders affecting different tissue types. One prime target for delivering therapeutic transgenes using AAV is the central nervous system (CNS). In particular, CNS-targeted AAV vectors are being evaluated for treating a broad range of monogenic and neurodegenerative diseases afflicting the CNS, e.g., spinal muscular atrophy (SMA), Parkinson's, Alzheimer's, Friedrich's ataxia, and several

Citation Albright BH, Simon KE, Pillai M, Devlin GW, Asokan A. 2019. Modulation of sialic acid dependence influences the central nervous system transduction profile of adeno-associated viruses. *J Virol* 93:e00332-19. <https://doi.org/10.1128/JVI.00332-19>.

Editor Rozanne M. Sandri-Goldin, University of California, Irvine

Copyright © 2019 American Society for Microbiology. All Rights Reserved.

Address correspondence to Aravind Asokan, aravind.asokan@duke.edu.

Received 25 February 2019

Accepted 11 March 2019

Accepted manuscript posted online 20 March 2019

Published 15 May 2019

lysosomal storage diseases, to name a few (1). Understanding AAV-host interactions, particularly within the context of the CNS at the mechanistic level, can help guide optimal design of recombinant AAV vectors for such therapeutic applications (2, 3).

AAV is a small, nonpathogenic, helper-dependent virus of the family *Parvoviridae* with a 4.7-kb single-stranded DNA (ssDNA) genome (4). A wide array of both natural isolates and synthetic variants have been developed as recombinant vectors which display broad tropisms across the host species, tissue, and cellular levels (5, 6). These functional attributes are determined by capsid structural features and capsid-host factor interactions. The AAV capsid is a small (~25 nm) T=1 icosahedron composed of 60 viral protein (VP) monomers (VP1, VP2, and VP3 variants, assembled in a ratio of 1:1:10, respectively). The VP monomer is characterized by a conserved jellyroll, β -barrel structure that is comprised of seven antiparallel β -strands (7). The interdigitating loop regions connecting these strands are highly variable regions (VRs) in sequence and highly plastic, being amenable to modification/mutation. Furthermore, these surface-exposed loops determine the topology of the capsid surface and have a profound effect on virus-host interactions, dictating receptor usage, antigenicity, tissue tropism, and species specificity (8, 9).

Principal among these virus-host interactions is the recognition of specific glycans, which serve as attachment factors (10, 11). Binding of the AAV capsid to cell surface glycans serves as the initial step in the life cycle of AAV and is followed by subsequent interactions with the universal AAV receptor (AAVR) during endocytic uptake, intracellular trafficking steps, and nuclear entry leading to transduction (9). Various glycans recognized by AAV serotypes have been identified. Examples include recognition of heparan sulfate (AAV2 and AAV3 [AAV2/3]), sialic acid (SIA; AAV1/4/5/6), galactose (AAV9), and N-acetyl lactosamine (LacNAc; AAVrh.10) (11). Specifically, AAV1 and AAV6 recognize both α 2,3 and α 2,6 N-linked SIA, while AAV5 also recognizes N-linked SIA, while AAV4 uniquely recognizes α 2,3 O-linked SIA (mucin). From a structural perspective, the structures of various AAV capsids complexed with their cognate glycans have further pinpointed glycan binding sites to the protrusions at the 3-fold axis of symmetry on the capsid. The residues and locations on the AAV capsid surface that influence such interactions, referred to as glycan binding footprints, are now known for AAV1, -2, -3, -4, -5, -6, and -9 (11–14).

Different AAV serotypes exhibit various CNS tropisms, and our understanding of the role of glycans in dictating these cellular tropisms is expanding. CNS tropism and transduction profiles can vary drastically based on the route of AAV administration in different hosts (e.g., intravascular, intracerebrospinal fluid [CSF], or intraparenchymal). Notably, certain serotypes, AAV9, AAVrh.8, and AAVrh.10, are able to traverse the blood-brain barrier (BBB) following systemic administration and enter the brain parenchyma to efficiently transduce cells within the CNS (15, 16). However, the capsid-glycan interactions that might influence the mechanisms underlying AAV capsid transport across the BBB into the CNS are not well understood. Toward furthering this understanding, our lab recently identified structural determinants on the AAVrh.10 capsid, which when grafted onto the AAV1 capsid (AAV1RX) permits CNS entry (17). The engineered AAV1RX variant demonstrates marked transduction of neurons across multiple brain regions and reduced tropism for glial and vascular endothelial cells in the brain. To further understand the mechanisms underlying such transendothelial transport into the CNS, we extensively characterized several AAV capsid variants displaying a range of SIA interactions in the current study. We postulate a model wherein the glycan dependence of AAV capsids inversely correlates with their ability to transduce cells in the CNS.

RESULTS

Characterization of AAV capsid variants spanning the SIA sensitivity spectrum.

We hypothesized that altered SIA interactions might be involved in the mechanism by which AAV1RX is able to cross the BBB and transduce cells within the brain parenchyma. To investigate such a relationship, we first selected several AAV capsid variants

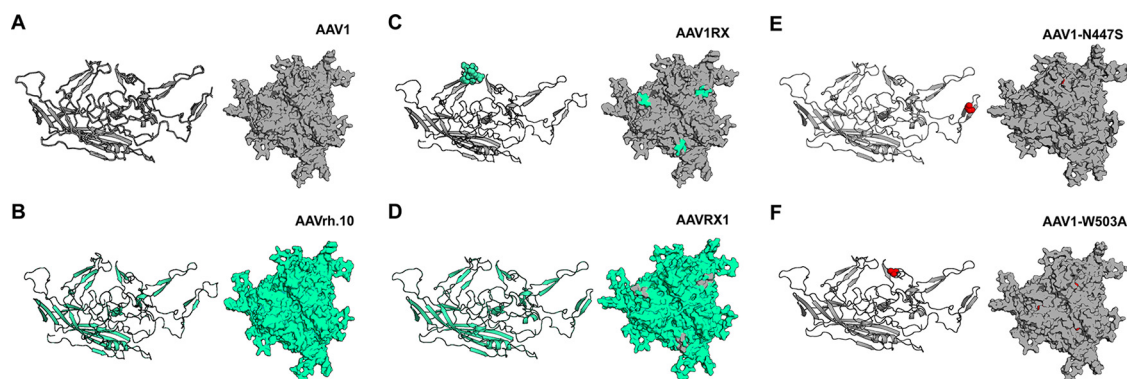


FIG 1 Structural models of AAV1, AAVrh.10, and mutant capsids evaluated in this study. Three-dimensional molecular models of different AAV VP3 monomers and trimers were generated for each wild-type and mutant capsid, as follows: AAV1 (A), AAVrh.10 (B), AAV1RX (AAV1 capsid VP3 replaced with variable region 1 [VR1] from AAVrh.100) (C), AAVRX1 (AAVrh.10 capsid VP3 replaced with VR1 from AAV1) (D), AAV1-N447S (E), and AAV1-W503A (F). Amino acid residues derived from AAV1 are shown in gray, residues derived from AAVrh.10 are depicted in green, and single amino acid substitutions (AAV1-N447S and AAV1-W503A) are shown in red. These structural models were generated using SWISS-MODEL and PyMOL.

possessing differential affinities for binding α 2,3 and α 2,6 N-linked sialic acid (SIA), the primary glycan attachment factor for AAV1. First, we included AAV1RX, as well as its parental serotypes, AAV1, which strongly depends on SIA (18), as a positive control, and AAVrh.10, which does not bind SIA, as a negative control (Fig. 1A). Further, we generated the AAVRX1 capsid variant to further interrogate the AAV1RX capsid footprint, by performing the reciprocal swap relative to AAV1RX (Fig. 1B). Briefly, AAV1RX was generated by grafting a stretch of 8 residues from the variable region 1 (VR1) of AAVrh.10 onto the AAV1 capsid. Specifically, these residues were 263N, 264G, 265T, 266S, 268G (an insertion relative to the AAV1 sequence), 269S, 270T, and 274T. In contrast, AAVRX1 was generated by substituting the corresponding residues from AAV1 (262S, 263A, 264S, 265T, 266G, a deletion at position 267 relative to the AAVrh.10 sequence, 268A, and 269S) for residues in the AAVrh.10 backbone. Additionally, we generated two AAV1-based capsid mutants harboring single amino acid substitutions, AAV1-N447S and AAV1-W503A, in which the asparagine at position 447 (AAV1 VP1 numbering) was replaced by serine and in which the tryptophan at position 503 was replaced by an alanine, respectively (Fig. 1C and D). These mutations have been previously reported, and both the asparagine at position 447 and the tryptophan at position 503 have been shown to be located within the AAV1 SIA binding pocket and play a direct role in binding SIA as direct contact residues (14). Accordingly, these mutations have both been shown to result in diminished SIA binding for AAV1. Structural models of these capsid variants, showing both the full capsid (60-mer) as well as the 3-fold axis of symmetry/trimer, are shown in Fig. 1.

We first evaluated the infectivity of these capsid variants by performing *in vitro* transduction assays on three biologically relevant CNS-derived cell lines: the Neuro2a mouse neuroblastoma cell line, the U87 human astrocytoma cell line, and the MB114 mouse brain microvascular endothelial cell line (Fig. 2). These cells were infected with each capsid variant at a multiplicity of infection (MOI) of 10,000 vector genomes (vg)/cell, and infection was carried out for 48 h. In the case of the Neuro2a cell line, transduction by most capsid variants seemed to phenocopy either AAV1, producing relatively high transduction levels, or AAVrh.10, demonstrating transduction levels that were roughly 1 log-fold lower (Fig. 2A). The two groups are separated by a dotted line in the figure. Despite some variation in transduction levels, the overall transduction profiles observed for the U87 cell line were similar, again yielding two groups (dotted line), behaving either more AAV1-like or more AAVrh.10-like (Fig. 2B). Only in the case of the MB114 mouse brain microvascular cell line did we see these capsid variants demonstrate a more intermediate phenotype (between dotted lines), showing substantial (~ 0.5 to 1.5 log-fold) differences relative to the level with either AAV1 or

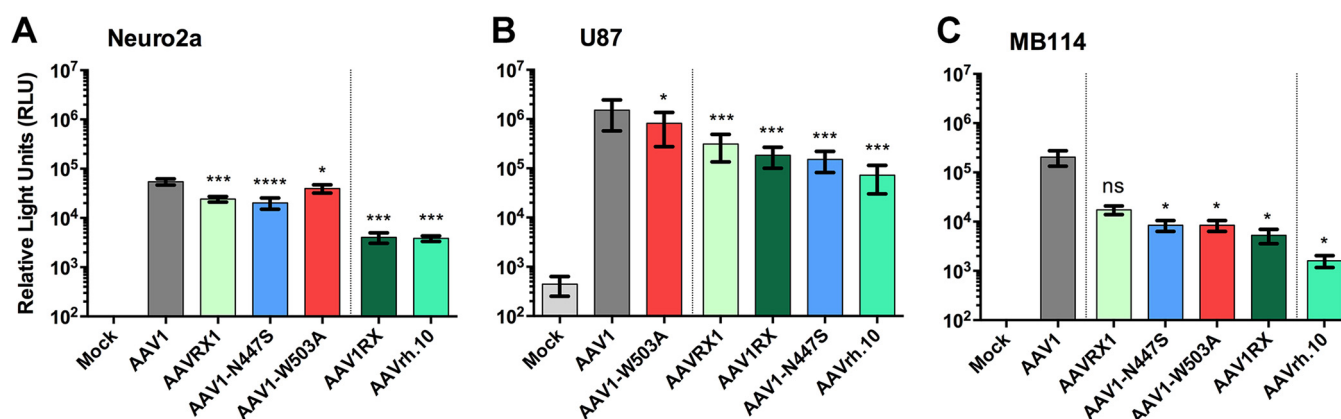


FIG 2 Transduction profiles of different AAV capsids in cultured cell lines representing CNS tissue composition. Neuro2a mouse neuroblastoma (A), U87 human glioma (B), and MB114 mouse brain microvascular endothelial (C) cells were incubated with AAV vectors packaging a luciferase transgene at 10,000 vg/cell. Cells were lysed at 48 h postinfection to measure luciferase reporter expression. Dotted lines separate capsids into functional subgroups based on relative transduction efficiencies. Data are presented as means, and error bars represent standard deviations ($n = 3$) from biological replicates. For transduction, an unpaired two-tailed t test with Welch's correction was performed to demonstrate statistical significance. ns, not significant; *, $P < 0.05$.

AAVrh.10. Based upon this observation, as well as upon the physiological relevance in terms of the BBB, we selected the MB114 brain microvascular cell line for further experiments to assess the dependency of these capsids on sialic acid for cell surface attachment and transduction.

Capsid variants display differential sensitivities to removal of cell surface SIA.

We next wanted to evaluate the dependency of these capsids on the presence of cell surface SIA. To do so, we performed *in vitro* transduction assays on MB114 cells following pretreatment with either serum-free medium (as a negative control) or with 50 mU/ml of neuraminidase (type III, from *Vibrio cholerae*), which enzymatically removes terminal sialic acid residues from the cell surface (Fig. 3A). As expected, AAV1 was highly sensitive to removal of cell surface SIA, resulting in a roughly 1.5-log decrease in transduction following treatment. In contrast, AAVrh.10, which binds LacNAc (19), did not appear to depend upon cell surface SIA for transduction as treatment with neuraminidase had no effect on transduction. Similarly, both AAVRX1 and AAV1-N447S transduction appeared to be SIA independent as they were unaffected by neuraminidase treatment. However, a third functional group could be observed for other capsid variants. Both AAV1RX and, to a slightly lesser extent, AAV1-W503A demonstrated an intermediate sensitivity to enzymatic removal of cell surface SIA with a moderate yet significant decrease in transduction levels (roughly 2-fold and 1.5-fold, respectively).

Having observed differential sensitivities of these capsid mutants to enzymatic removal of cell surface SIA in terms of transduction levels, we next wanted to determine whether this finding would correlate to cell surface binding of virions. Thus, we performed binding assays measuring the number of viral genomes bound per cell and plotted the data as fold change following desialylation using neuraminidase treatment (Fig. 3B). Consistent with the transduction profile, AAV1 binding was found to be highly dependent on the presence of SIA as desialylation resulted in a nearly 2-log decrease in the number of bound viral genomes per cell. Further, AAVrh.10 binding appears to be independent of SIA as desialylation did not result in any decrease in the number of bound virions detected per cell. Likewise, cell surface attachment for both AAV1-N447S and AAVRX1 does not depend on the presence of SIA. Last, the intermediate functional group identified in the transduction assays is recapitulated here as well: AAV1RX and, again, to a lesser degree, the AAV1-W503A mutant both showed moderate sensitivities to removal of cell surface SIA, demonstrating roughly a 1.25-log-fold and near-log-fold decrease in the number of bound viral genomes following neuraminidase treatment. To summarize, AAV1, the sole capsid in functional group I, binds SIA with relatively high affinity while the capsids in group III, AAVrh.10, AAVRX1, and AAV1-N447S, do not

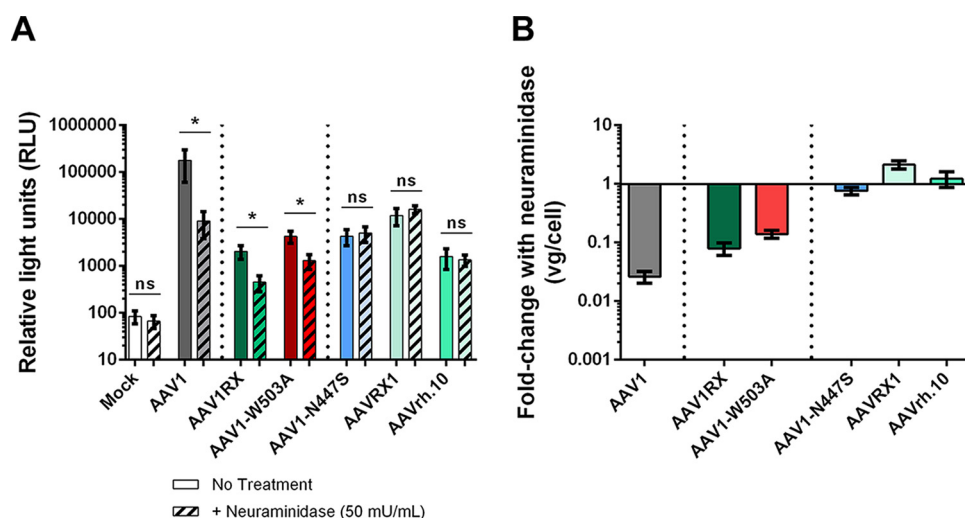


FIG 3 Sialic acid dependence of different AAV capsids for cell surface attachment and transduction. (A) Transduction efficiencies of AAV capsids on MB114 cells following a 2-h pretreatment with either serum-free medium or serum-free medium containing 50 mU/ml neuraminidase (type III, from *Vibrio cholerae*). Viruses packaging a CBA-Luc reporter gene were incubated on MB114 cells (MOI of 10,000 vg/cell) immediately following treatment. Cells were assessed at 48 h postinfection to measure relative luciferase transgene expression. Patterned bars represent transduction following treatment with neuraminidase. (B) Fold change in cell surface attachment of different AAV capsids on MB114 cells upon neuraminidase treatment. Cells were treated with neuraminidase, prechilled prior to incubation with virus for 1 h at 4°C, following which bound viruses were quantified by qPCR. Dotted lines separate capsids into functional subgroups reflecting sensitivity to neuraminidase. Data are presented as means \pm standard errors of the means ($n = 3$ or higher) from biological replicates. For transduction, an unpaired two-tailed t test with Welch's correction was performed to demonstrate statistical significance. ns, not significant; *, $P < 0.05$.

possess any capacity to bind SIA. Furthermore, these data suggest that both of the capsids in functional group II, AAV1RX and AAV1-W503A, retain the ability from their parental AAV1 to recognize SIA; however, their affinity for SIA is reduced, with AAV1-W503A showing an even greater reduction in SIA binding affinity than AAV1RX.

SIA dependence inversely correlates with CNS transduction. Having observed these different functional groups in terms of sensitivities to enzymatic removal of cell surface terminal SIA residues from *in vitro* transduction and binding assays, we next wanted to see if these results would correlate with *in vivo* transduction assays. In particular, we hypothesized that differential SIA binding affinities displayed by these capsid mutants would correlate with differential capacities for CNS tropism/transduction following systemic administration. Thus, we administered AAV1, AAVrh.10, AAV1RX, or one of the two mutant capsids, AAV1-N447S or AAV1-W503A, packaging a chicken beta actin hybrid-green fluorescent protein (CBh-GFP) reporter cassette at a dose of 5×10^{11} vg per mouse ($\sim 2.5 \times 10^{13}$ vg/kg) via tail vein injections in C57BL/6 mice. Additionally, we also administered the reciprocal swap variant, AAVRX1, at the same dose in order to evaluate the 1RX footprint outside the context of SIA interactions via ablation of the footprint on AAVrh.10. At 21 days postinjection, mice were sacrificed, tissues were removed and processed, and 50- μ m coronal brain sections were immunostained for GFP. These sections were then scanned under bright-field conditions at $\times 20$ magnification, and representative images were taken from multiple brain regions in order to assess GFP transgene expression throughout the brain parenchyma. We have included representative images for multiple brain regions, including the cerebral cortex, showing both the somatosensory cortex (SCT) (Fig. 4A) and the motor cortex (MCT) (Fig. 4B). We also evaluated transduction profiles in the hippocampus, visualizing CA1 and CA2 (CA1/2) pyramidal neuron layers (Fig. 4C) and the dentate gyrus (DG) (Fig. 4D). We assessed transduction in the striatum (caudoputamen) region of coronal lateral ventricle sections (Fig. 4E). We also visualized transduction in the thalamus (Fig. 4F)

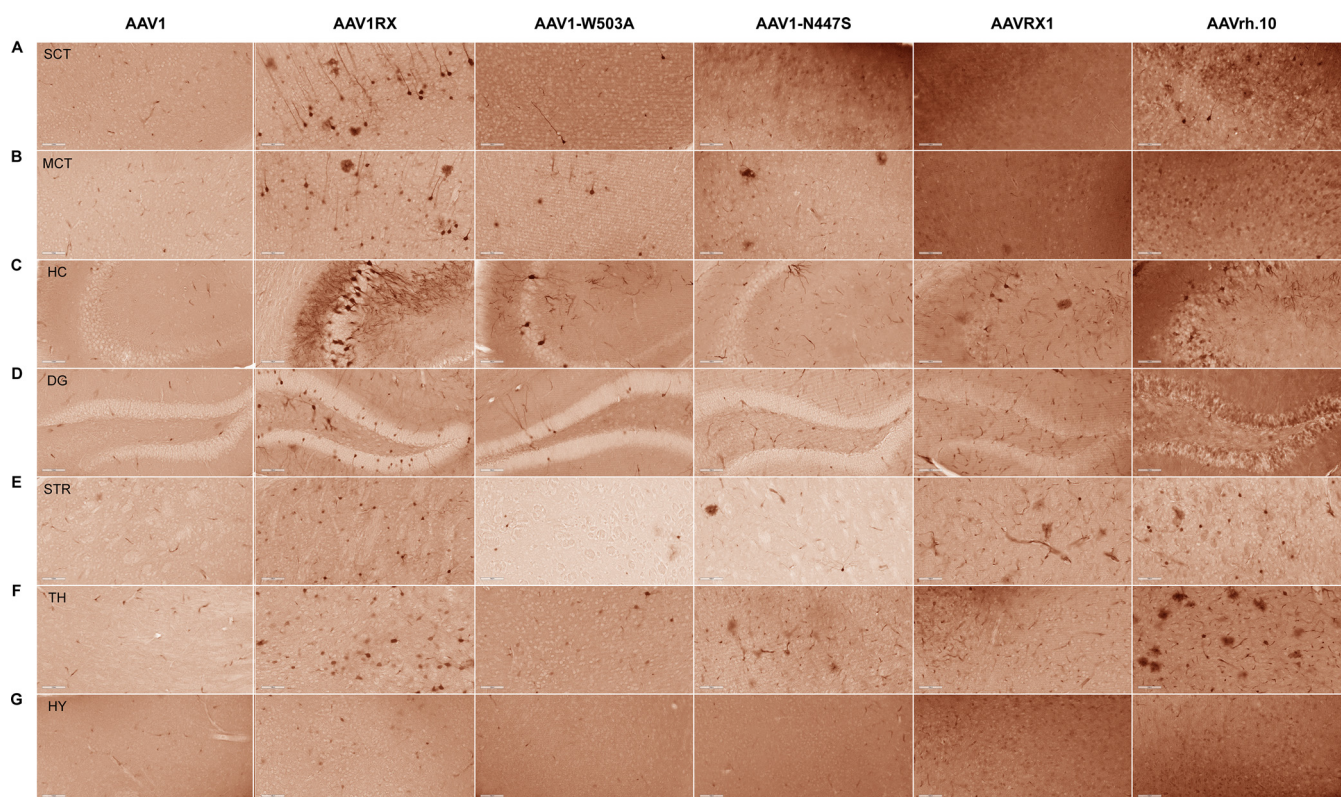


FIG 4 *In vivo* CNS transduction profiles of different AAV capsid variants. Vectors packaging a self-complementary GFP transgene cassette were administered intravenously in C57BL/6 mice at a dose of 5×10^{11} vg/mouse, and immunohistochemistry was carried out at 21 days postinjection. Vectors are indicated at the top of the scans, and regions are indicated on the left. (A) SCT, somatosensory cortex; (B) MCT, motor cortex; (C) HC, pyramidal neurons of the hippocampus; (D) DG, dentate gyrus; (E) STR, striatum (caudoputamen); (F) TH, thalamus; (G) HY, hypothalamus. Representative images from different mouse cohorts ($n = 3$ or higher) are shown. Vasculature (black arrows) and astrocytes (black arrowheads) are highlighted. Scale bar, 100 μ m.

and hypothalamus (Fig. 4G). Qualitative trends in these regions are further corroborated by quantitations of GFP-positive (GFP⁺) neurons and glia in the cortex (CTX) (Fig. 5A), the hippocampus (HC) (Fig. 5B), and the striatum (STR) (Fig. 5C).

AAV1, which is a capsid highly dependent on SIA interactions, fails to transduce the CNS. We observed that following intravascular administration, AAV1 transduction is limited to microvascular endothelial cells across each region of the brain that we evaluated. Negligible numbers of GFP⁺ neurons and glial cells were observed, regardless of brain region, emphasizing the known vascular sequestration phenotype for AAV1.

AAVrh.10 is not SIA dependent and is characterized by its ability to efficiently enter and transduce the CNS. Thus, AAVrh.10 was included as a positive control for systemic CNS transduction (15). Accordingly, AAVrh.10 demonstrated robust transduction of neurons, glia, and vascular endothelial cells across the cerebral cortex, including the SCT (Fig. 4A) and the MCT, as well as for overall quantitations of cortical expression (Fig. 5A). In the case of AAVrh.10, we also observed substantial variation in terms of the intensity of immunostained GFP⁺ cells, contributing to the variation we observed in the number of GFP⁺ cells across brain sections from different mice. Interestingly, we also frequently observed a pronounced gradient in terms of transduced cortical neurons in the cortex (Fig. 4A and B). Specifically, we observed a high density of GFP⁺ neurons in cortical layers 1 to 3, which lie at the periphery of the parenchyma, which decreased across layers 4 to 6. This observation is consistent with previous studies performed by our lab. Similarly, AAVrh.10 transduced neurons, glia, and endothelial cells in the hippocampus, including pyramidal neuron layers (Fig. 4C) and the DG (Fig. 4D), as well as for overall levels of hippocampal neuron and glial expression (Fig. 5B). AAVrh.10 transduced all cell types with high efficiency, indicating efficient capsid entry into the

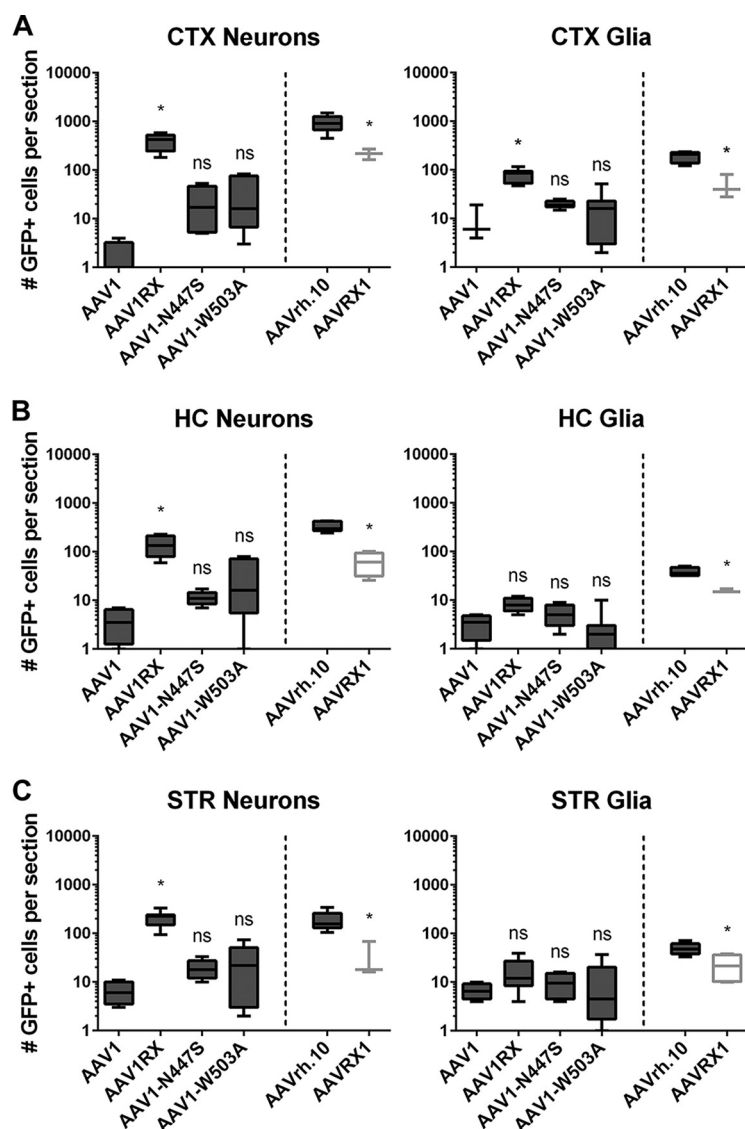


FIG 5 Quantitation of neuronal and glial transduction profiles of different AAV capsids. Brain sections were immunostained and imaged using a slide scanner, and the number of GFP⁺ neurons/glia was quantified as determined by cellular morphology in cerebral cortex (A), hippocampus (B), and striatum (C). Mean values are shown, and error bars represent standard deviation ($n = 3$ or higher). ns, not significant; *, $P < 0.05$.

STR (Fig. 4D and 5C), as well as within both the thalamus (Fig. 4E) and the hypothalamus (Fig. 4F).

AAV1RX is moderately dependent on SIA for binding, efficiently enters the CNS, and efficiently transduces neurons. Upon systemic administration, we observed high levels of neuronal transduction across the somatosensory (Fig. 4A) and motor cortices (Fig. 4B). Neuronal expression levels were only marginally lower than those observed for AAVrh.10 across the entire cortex, while AAV1RX demonstrated a 2-fold decrease in glial transduction alongside greatly diminished vascular transduction relative to that of AAVrh.10 (Fig. 5A). Again, AAV1RX recapitulated previously reported data (17), showing robust neuronal transduction at levels only marginally lower than those for AAVrh.10 in the hippocampus while transducing ~5-fold-fewer glial cells than AAVrh.10 (Fig. 5B). This trend was evident for both pyramidal neuronal layers (Fig. 4C) and granular layers in the dentate gyrus (Fig. 4D). We saw a similar trend in other brain regions, where we observed a robust number of GFP⁺ neurons with relatively fewer

GFP⁺ glia in the striatum (Fig. 4E) and thalamus (Fig. 4F). In the hypothalamus, however, AAV1RX seemed to transduce lower levels of both neurons and glia (Fig. 4G). Whereas in other brain regions we saw a modest decrease in AAV1RX neuronal transduction levels compared to the level for AAVrh.10, AAV1RX transduced striatal neurons at levels equal to those of AAVrh.10 while simultaneously showing a greater than 2-fold decrease in glial transduction (Fig. 5C).

AAV1-N447S and AAV1-W503A are capsid mutants with defective SIA binding and demonstrate low CNS transduction levels. We next wanted to evaluate two AAV1-based mutants with mutations in the SIA binding footprint (14). AAV1-W503A demonstrated a moderate (although further diminished relative to the level of AAV1RX) dependency on SIA interactions for *in vitro* transduction and binding. The other capsid mutant, AAV1-N447S, which does not bind SIA, was evaluated in tandem. Both mutants, when injected intravenously, demonstrated increased neuronal and glial transduction levels relative to the level of AAV1, as evidenced by roughly 20-fold and 2-fold increases in the numbers of GFP⁺ cortical neurons and glia detected, respectively (Fig. 5A). Interestingly, we also observed lower levels of vascular transduction for AAV1-W503A; however, AAV1-N447S mediated considerable GFP expression in the vasculature. (Fig. 4A and B). Despite an observable increase in the amount of GFP⁺ neurons and glia in the cortex relative to AAV1, mean AAV1-W503A and AAV1-N447S transduction levels averaged only ~5 to 8% and ~22 to 25% of those observed for AAV1RX for neurons and glia, respectively. Throughout the hippocampus, the SIA binding-defective mutants showed the same general trend across pyramidal neuron layers (Fig. 4C) and the dentate gyrus (Fig. 4D). Both mutants mediated roughly equivalent neuronal transduction levels, i.e., ~3- to 8-fold higher than AAV1, and glial transduction levels equivalent to those of AAV1 (Fig. 5B). Nonetheless, there were significantly fewer GFP⁺ hippocampal neurons observed for both mutants relative to the level for AAV1RX, which demonstrated an approximately log-fold-higher expression in neurons and approximately a half-log difference in the number of transduced glia.

In the striatum, both mutants mediated roughly equivalent transduction profiles compared to other brain regions although more sample-to-sample variation was seen for AAV1-W503A, consistent with its greater, yet modest, SIA dependence (Fig. 4E). Here, we saw a modest increase in transduction levels for both mutants relative to the level of AAV1, with ~3- to 4-fold-higher numbers of GFP⁺ striatal neurons and ~1.5-fold more GFP⁺ glia (Fig. 5C). Nonetheless, a significant log-fold decrease in the number of GFP⁺ striatal neurons was observed for AAV1-N447S and AAV1-W503A compared to the level for AAV1RX (Fig. 5C). Consistent with the results described above, few GFP⁺ neurons and glia were seen for either mutant in the thalamus, indicating only marginal improvement in CNS transduction relative to the level for the wild-type AAV1 capsid (Fig. 4F). Last, few GFP⁺ neurons or glia were seen in the hypothalamus for either mutant, while low to moderate levels of vascular transduction were seen in the hypothalamus for all capsid variants. In general, we observed a trend in which SIA dependence seemed to inversely correlate with CNS entry and transduction of the brain parenchyma.

AAVRX1, the reciprocal swap relative to AAV1RX, demonstrates attenuated CNS transduction relative to that of AAVrh.10. Last, we evaluated AAVRX1, the other remaining capsid variant that does not bind SIA. Across the cortex, we saw that intravascularly administered AAVRX1 did transduce neurons and glia in the brain, as observed in the somatosensory (Fig. 4A) and motor (Fig. 4B) regions of the cortex; however, these transduction levels were markedly reduced, with ~22% and ~26% of the number of GFP⁺ cortical neurons and glia, respectively, compared to the levels observed for AAVrh.10 (Fig. 5A). AAVRX1 also transduced the brain microvasculature similarly to AAVrh.10, as assessed visually (Fig. 4). Interestingly, we found that AAVRX1 seemed to phenocopy AAVrh.10 in terms of the aforementioned gradient in the density of GFP⁺ cells across cortical neuron layers; furthermore, we saw an even greater number of more faintly stained GFP⁺ cells than for AAVrh.10. AAVRX1 exhibited a significant log-fold decrease in neuronal transduction and a 2-fold decrease in glial

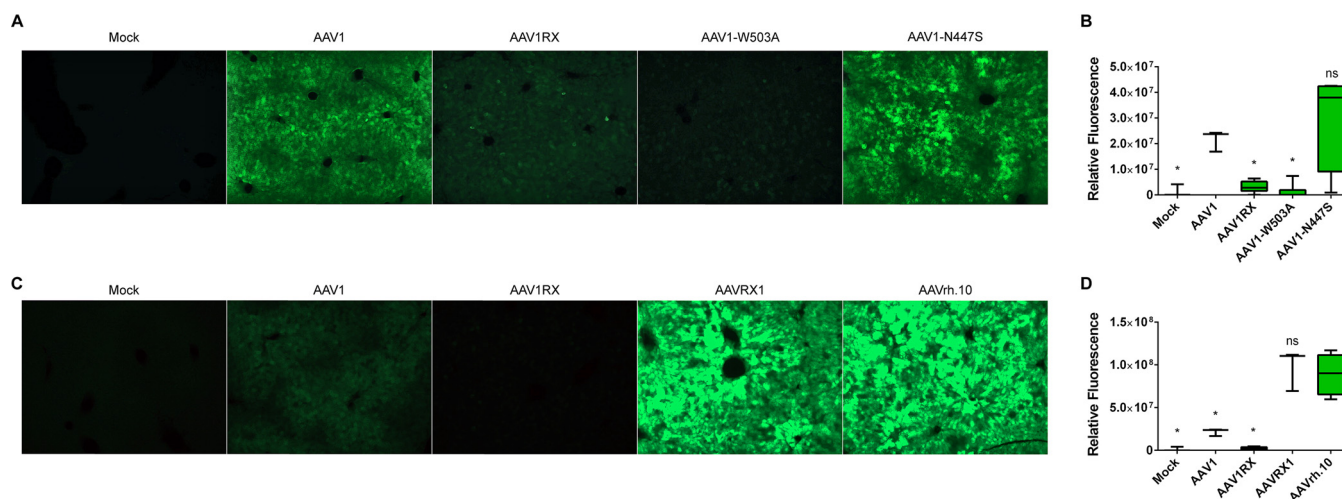


FIG 6 Liver transduction profiles of different AAV capsids. At 3 weeks postinjection of different AAV-scGFP vectors, liver sections were immunostained and imaged using fluorescence microscopy. GFP expression was imaged at 10% light intensity for the mock cohort, AAV1, AAV1RX, AAV1-W503A, and AAV1-N447S (A), and relative fluorescence was quantified with ImageJ and averaged across multiple images per section per liver sample ($n = 10$ or higher) (B). In addition, GFP expression was imaged at 1% light intensity for the mock cohort, AAV1, AAV1RX, AAVRX1, and AAVrh.10 (to avoid oversaturation of signal) (C), and relative fluorescence was quantified with ImageJ and averaged across multiple images per section per liver sample ($n = 10$ or higher) (D). Data as represented as means \pm standard deviations ($n = 3$ or higher). One-way ANOVA followed by Tukey's multiple-comparison test was carried out to demonstrate statistical significance for results for either AAV1 or AAVrh.10 relative to the data in panel B or D, respectively. ns, not significant. *, $P < 0.05$.

transduction relative to levels for AAVrh.10 in both the hippocampus (Fig. 4C and D and 5B) and the striatum (Fig. 4E and 5C). Last, while AAVRX1 continued to show noticeably fewer GFP-negative neurons and glia than AAVrh.10 in the thalamus (Fig. 4F), it appeared to behave similarly to AAVrh.10 in the hypothalamus, showing similar albeit slightly lower numbers of GFP⁺ hypothalamic neurons and similarly sparse GFP⁺ glia (Fig. 4G).

Effect of SIA dependence on liver tropism and transduction. In comparison with AAV1, which transduces the liver with moderate efficiency, AAVrh.10 is known to exhibit pronounced hepatotropism following intravenous administration and mediates very high liver transduction (20, 21). Our lab recently showed that upon intravenous injection in mice, AAV1RX was detargeted from the liver despite maintaining robust CNS transduction (17). Having shown that AAV1RX demonstrated reduced SIA dependence *in vitro*, which correlates with its CNS phenotype, we hypothesized that interference with capsid-SIA interactions could also explain the decreased liver tropism and transduction observed in the case of AAV1RX. Briefly, we evaluated GFP reporter expression in liver samples from mice that were intravenously injected with either AAV1, AAVrh.10, AAV1RX, AAVRX1, AAV1-N447S, or AAV1-W503A, each packaging a CBh-GFP reporter cassette, at a dose of 5×10^{11} vg/mouse. Liver sections were immunostained for GFP reporter expression and were imaged using a fluorescence microscope to assess GFP transgene expression (Fig. 6A and C). GFP expression was then quantified using ImageJ software in order to measure average fluorescence for multiple images per mouse (Fig. 6B and D). Consistent with previous studies, we observed moderate GFP expression levels for AAV1 and extremely low GFP expression for AAV1RX in the liver. Next, we evaluated AAV1-W503A, which displayed further reduced yet still moderate SIA dependence relative to that of AAV1RX. Consistently, AAV1-W503A also exhibited extremely low GFP expression in the liver and was similarly liver detargeted relative to the level for AAV1 (Fig. 6A and B). Interestingly, the AAV1-N447S mutant, which, unlike the W503A mutation, exhibited complete independence from SIA interactions for *in vitro* transduction and binding, was not liver detargeted. AAV1-N447S actually showed increased GFP expression in the liver relative to that of AAV1 although substantial variability in GFP expression levels was observed across different tissue samples (Fig. 6B).

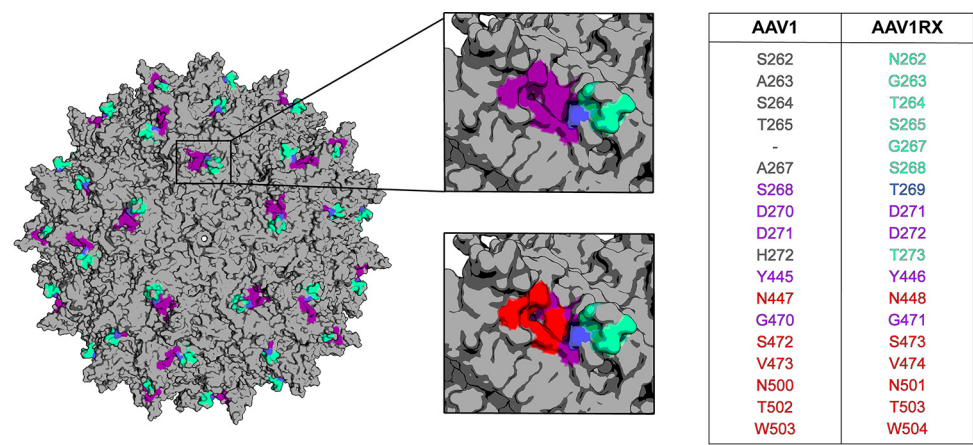


FIG 7 Structural analysis of the AAV1RX footprint. Three-dimensional capsid surface model of AAV1RX overlaying key residues within the AAV1 sialic acid (SIA) binding footprint onto residues from the AAVrh.10 VR1 region that were swapped onto AAV1 (AAV1RX). AAV1-derived residues are depicted in gray, the eight residues of the 1RX footprint are depicted in green, the residues of the AAV1 SIA binding footprint are shown in magenta, residues shared between the SIA receptor footprint and the 1RX region are shown in blue, and residues in direct contact with SIA are shown in red. Homology models were generated using Swiss-Model; oligomers generated using VIPERdb and PyMol were used to generate surface-rendered capsids. Amino acid residues and their positions with VP numbering are listed adjacent to the structures.

We also evaluated the transduction profile for AAVRX1 in the liver alongside AAV1, AAV1RX, and AAVrh.10. As expected, the hepatotropic AAVrh.10 capsid exhibited extremely high GFP expression in the liver. Interestingly, despite having exhibited attenuated CNS transduction, AAVRX1 was found to retain the liver tropism of its parental AAVrh.10 capsid. GFP expression levels for AAVRX1 in the liver were equal to or higher than those for AAVrh.10 (Fig. 6C and D). Because of oversaturation of the fluorescent signal due to the extremely high intensity of GFP expression observed for AAVrh.10 and AAVRX1, we captured images using a lower (1%) intensity setting on the microscope, and these representative images are shown in a separate panel (Fig. 6C) with the images taken at a higher-intensity setting (10%), shown in Fig. 6A. All quantifications of relative fluorescence, however, were measured using images captured at the 10% intensity setting.

Structural analysis of key AAV1RX capsid residues within the context of the AAV1 SIA binding pocket. We recently mapped the functional correlates of an AAV1RX surface footprint consisting of 8 key amino acid residues (263N, 264 G, 265T, 266S, 268 G [an insertion relative to wild-type AAV1], 269S, 270T, and 274T [VP1 numbering, relative to AAV1]) located within variable region 1 (VR1), the loop connecting β strands B and C in the VP monomer. As previously described, these residues are exposed on the surface of the full 60-mer capsid and manifest as a cluster located on a protruding shoulder region located near the base of the larger protrusions at the 3-fold axis of symmetry (22, 23). This capsid structural feature serves as a hot spot for determining species, tissue, and cellular tropism as well as antigenicity. This shoulder region containing specific AAV1RX residues is also located in close proximity to and at the edge of the depression at the 2-fold axis of symmetry.

Based on recent structural studies (14), we modeled the SIA binding pocket on AAV1, containing 11 amino acid residues (S268, D270, N271, Y445, N447, G470, S472, V473, N500, T502, and W503; AAV1 Vp1 numbering) and located at the base of the 3-fold spikes. On the capsid monomer, these residues span VR1, VR4, and VR5 regions. We generated models of the AAV1RX capsid on which we overlaid the AAV1 SIA binding pocket residues (Fig. 7, magenta) with the AAV1RX footprint residues (cyan). From this overlay, we saw that a single amino acid residue overlapped the two footprints (pale blue), a serine at position 268 (S268) in the AAV1 sequence, which has been mutated to a threonine in the AAV1RX footprint (270T; AAV1RX VP1 numbering).

Of the aforementioned 11 residues of the AAV1 SIA binding pocket, only 6 residues have been implicated as direct contact residues for binding the glycan; these are N447, S472, V473, N500, T502, and W503 (again, AAV1 VP1 numbering). The other five residues (S268, D270, N271, Y445, and G470) play an indirect role in mediating capsid-SIA interactions. When overlaid with the 1RX footprint, the single overlapping residue that has been mutated in the SIA binding pocket, S268T (AAV1, VP1 numbering), is not directly involved in binding SIA, but still impacts capsid-SIA interactions. Furthermore, we see in our structural model that this overlapping (Fig. 7, blue) residue lies nearby but not directly at the mouth of the binding pocket by the 3-fold spike (Fig. 7, top inset). Additionally, we highlighted the six direct contact residues for SIA in red (Fig. 7, bottom inset). Within this region residues directly involved in binding SIA were mutated in the AAV1-W503A and AAV1-N447S substitutions that were evaluated in this study. We observed that single amino acid substitutions of these direct SIA contact residues resulted in greatly diminished SIA binding or abolished SIA binding for the W503A and N447S mutants *in vitro*, respectively. In conclusion, the AAV1RX footprint appears to have optimally engineered SIA recognition, which contributes to efficient CNS entry and transduction.

DISCUSSION

AAV serotypes utilize a broad range of cell surface glycans for attachment, which are, in part, key determinants of tropism (11). In particular, several AAV serotypes recognize different forms of SIA, with AAV1 binding α -2,3 and α -2,6 N-linked SIA within a pocket of residues located at the base of the 3-fold capsid surface protrusions. Systemic administration of AAV1 results in a largely vascular and hepatic transduction profile, with negligible CNS transduction (20). However, engraftment of the 1RX footprint from AAVrh.10 onto the AAV1 capsid enables efficient BBB transport and robust neurotropism/CNS transduction, along with reduced vascular and peripheral tissue transduction (17).

Structural analysis revealed that the eight residues of the 1RX footprint lie adjacent to the AAV1 SIA binding pocket located at the base of the 3-fold protrusions. Our data obtained from modifying residues adjacent to the SIA footprint rather than direct contact residues support the notion that partially attenuated SIA interactions might contribute to effective CNS transduction. Accordingly, we propose a Goldilocks model wherein the optimal SIA binding affinity, in conjunction with other contributing factors, can influence CNS tropism of AAV capsids. Specifically, capsids with strong SIA interactions show high levels of vascular transduction and low CNS gene transfer efficiency following systemic administration. Additionally, these capsids also transduce the liver efficiently. At the other end of the spectrum, capsids with either severely diminished or no SIA binding transduced the CNS with low-to-moderate efficiency, due to either reduced transport and/or transduction. The AAV1RX capsid displayed an intermediate SIA binding phenotype, whereby it effectively transduced cells in the brain parenchyma.

It is important to note that our proposed model, while sufficient to explain the phenotypes displayed by AAV1-based variants (and possibly other SIA binding serotypes), cannot directly address the mechanism utilized by AAVrh.10 in crossing the BBB. As mentioned earlier, AAVrh.10 has recently been shown to recognize sulfated LacNAc (19). It is likely that LacNAc interactions influence the CNS tropism of AAVrh.10 and that mutations in or around the LacNAc footprint could influence CNS transduction. Such a scenario is corroborated in part by the attenuated phenotype displayed by AAVRX1 (reciprocal swap of AAV1 VR1 residues onto AAVrh.10). Interestingly, however, AAVRX1 appears to retain the extremely high liver transduction phenotype of its parent. Another deviation from our model is the AAV1-N447S mutant, which despite abolished SIA dependence displayed improved AAV1-like transduction in the liver and vasculature. One possible explanation is that the AAV1-N447S change constitutes an amino acid change identical to that observed in AAVrh.10 at that same position, potentially

imparting AAVrh.10-like features. However, whether AAVrh.10 utilizes a footprint similar to that of AAV1-SIA capsids to recognize LacNAc glycans remains to be seen.

It is also important to note that capsid-glycan interactions offer only a partial explanation for AAV tropism in general and to acknowledge that other host receptors such as AAVR or soluble serum factors might play a critical role in this regard (24–27). Our understanding of AAV capsid interactions with serum factors is still evolving, wherein structural information and the impact of serum protein glycosylation on such interactions remain to be elucidated. However, it is worth highlighting the structural footprint for AAV2 capsid-AAVR interactions that was recently reported (28). Interestingly, residues within the VR1 region (S262, Q263, G265, A266, S267, N268, and H271) in one of the AAV2 VP3 monomer subunits play a significant role in determining capsid interactions with AAVR. Although the structural determinants of interactions between AAV1/AAVrh.10 and AAVR are yet to be determined, it is tempting to speculate that the AAV1RX and AAVRX1 chimeric capsids described here could display differential interactions with AAVR. Whether these interactions play a functional role in transport across the BBB or transduction of different cell types within the CNS remains to be determined.

Our observations are corroborated by several studies demonstrating that dependence on SIA glycans is inversely correlated with both virulence and spread for other viruses, such as other parvoviruses and polyomaviruses. This has been shown to be the case for the minute virus of mice (MVM), another parvovirus, which also recognizes α -2,3-sialylated glycans as a critical step for infection. Studies with SIA binding MVM mutants implicated differential SIA affinity as a key determinant of virulence in mice (29, 30). Similarly, differential SIA recognition and affinity have been reported as key factors influencing CNS tropism and pathogenicity of Theiler's virus, a picornavirus, as well as the systemic spread of polyomaviruses in mouse models (31–33). Another facet of the aforementioned studies that supports our conclusions is that similar SIA binding structural footprints, localized to the depression at the 2-fold axes of symmetry, appear to be employed by other parvoviruses, including MVM, canine parvovirus (CPV), and feline parvovirus (FPV) (30, 34–38). This region has now been established as a key determinant of glycan binding, antigenicity, tissue tropism, and BBB transport for different parvoviruses.

In summary, these results establish that capsid-glycan interactions can influence the CNS transduction profile of AAV capsids. While the current study hinges on AAV1 capsid variants and sialylated glycans as an example, it is plausible that other AAV serotypes and their cognate glycan attachment factors as well as other receptor(s) exhibit similar relationships that impact their CNS tropism. These findings also provide a structural basis for reengineering capsid-glycan interactions to achieve optimal CNS transduction.

MATERIALS AND METHODS

Generation of mutant AAV plasmid constructs. Mutant AAV plasmid constructs were cloned using site-directed mutagenesis via a QuikChange Lightning site-directed mutagenesis kit (catalog no. 200518; Agilent Technologies) according to the manufacturer's protocol. The following primer pairs were used to generate the single-amino acid changes onto the pXR1 (AAV1) backbone: for AAV1-N447S 5'-CCAATA CCTGTATTACCTGAGCAGAACTCAAAATCAG-3' (forward) and 5'-CTGATTTTGAGTTCTGCTCAGGTAATACAG GTATTGG-3' (reverse); for AAV1-W503A, 5'-CAACAGCAATTTTACCGCTACTGTGCTTCAAAATATAACC-3' (forward) and 5'-GGTTATATTTGAAGCACCAGTAGCGGTAAATGCTGTTG-3' (reverse). The following primer pair was used to generate the AAVRX1 mutant on the pXRrh.10 (AAVrh.10) backbone: 5'-CAGC AACGACAACCACTACTTCGGCTACAGACCCCTGG-3' (forward) and 5'-GCCCCCGTTGAAGCACTGGAGATT TGCTGTAGAGGTGGTTGTTGAGG-3' (reverse) (IDT Technologies, Ames IA).

Cell culture. HEK293 cells were cultured in Dulbecco's modified eagle medium (DMEM) supplemented with 10% fetal bovine serum (FBS) (Thermo Fisher, Waltham, MA) and 1% penicillin-streptomycin (P-S) (Thermo Fisher) in 5% CO₂ at 37°C. MB114 (mouse brain microvascular endothelial), U87 (human astrocytoma), and Neuro2a (mouse neuroblastoma) cell lines were all cultured as described above, except that they were cultured with DMEM supplemented with 5% FBS and 1% P-S. Gratefully, we received the MB114 cell line as a gift from Linda Van Dyk, University of Colorado.

Virus production and titers. Recombinant AAV vectors were produced using a triple plasmid transfection method consisting of a capsid-specific helper plasmid (i.e., pXR1, pXRrh.10, pXR-1RX, pXR-RX1, pXR1-N447S, or pXR1-W503A), an adenoviral helper plasmid (pXX680), and a transgene packaging cassette, encoding either self-complementary green fluorescent protein (scGFP) driven by a

chicken beta actin hybrid promoter (pTR-CBh-scGFP) or single-stranded luciferase driven by the chicken beta actin promoter (pTR-CBA-Luc), flanked by AAV2 inverted terminal repeat (ITR) sequences. Viral vectors were purified via iodixanol density gradient ultracentrifugation, subjected to phosphate-buffered saline (PBS) buffer exchange, and concentrated using Sartorius Vivaspin 6 (100-kDa-molecular-weight cutoff [MWCO]) centrifugation columns (F-2731-100; Bioexpress, Kaysville, UT). Titers of purified virus preparations were determined by quantitative PCR with primers amplifying the AAV2 ITR regions (forward, 5'-AACATGCTACGACAGAGGGAGTGG-3'; reverse, 5'-CATGAGACAAGGAACCCCTAGTGATGGA G-3') (IDT Technologies, Ames IA).

In vitro transduction assays. Different cell lines were seeded in 24-well plates at a density of 1×10^5 cells per well and allowed to adhere overnight at 37°C. The following day, cells were incubated with virus at a multiplicity of infection (MOI) of 10,000 vector genomes per cell and were incubated in 5% CO₂ at 37°C. At 48 h postinfection, cells were lysed using 150 μ l of $1 \times$ passive lysis buffer (Promega) for 20 min at room temperature. Fifty microliters of each cell lysate was then transferred to an assay plate, and luciferase reporter transgene expression levels were quantified using a Victor 3 multilabel plate reader (Perkin-Elmer) immediately after the addition of 50 μ l of luciferin (Promega) to each well.

Enzymatic desialylation assays. MB114 mouse brain microvascular endothelial cells were seeded in 24-well plates at a density of 1×10^5 cells per well and allowed to adhere overnight at 37°C. The following day, cells were pretreated with 50 mU/ml neuraminidase type III (from *Vibrio cholerae*) (N7885; Sigma) or with $1 \times$ PBS as a negative control, in serum-free DMEM at 37°C for 2 h. Cells were then washed three times with $1 \times$ PBS, given fresh DMEM containing 5% FBS and 1% P-S, and incubated with virus at an MOI of 10,000 vg/cell at 37°C. At 24 h postinfection, cells were lysed, and luciferase transgene expression levels were assayed as described earlier for the *in vitro* transduction assays.

Cell surface binding assays following enzymatic desialylation. MB114 mouse brain microvascular endothelial cells were seeded in 24-well plates at a density of 1×10^5 cells per well and allowed to adhere overnight at 37°C. The following day, cells were pretreated with 50 mU/ml neuraminidase type III (from *Vibrio cholerae*) (N7885; Sigma) in serum-free DMEM at 37°C for 2 h. Cells were then washed three times with $1 \times$ PBS and given fresh DMEM containing 5% FBS and 1% P-S. Cells were then prechilled at 4°C for 30 min prior to incubation with virus at an MOI of 10,000 vg/cell for 1 h at 4°C. Cells were then washed three times with ice-cold $1 \times$ PBS to remove unbound virions before adding 200 μ l of molecular biology-grade water to each well. Cells were subjected to three freeze-thaw cycles prior to collection of cell lysates along with cell surface-bound virions. Viral genome copy numbers of cell surface-bound virions were then quantified using quantitative PCR (qPCR) with primers specific to the luciferase transgene (forward, 5'-AAAAGCACTCTGATTGACAAATAC-3'; reverse, 5'-CCTTCGCTTCAAAAATGGAAC-3'). Viral genome copy numbers were then normalized to the mouse lamin B2 housekeeping gene using the following primer pair: forward, 5'-GGACCCAAGGACTACCTCAAGGG-3'; reverse, 5'-AGGGCACCTCCA TCTCGGAAAC-3'. The number of viral genomes is represented as the ratio of viral genomes/cell and were plotted as fold change relative to the level of the respective untreated control sample.

Animal studies. All animal experiments were performed using 6- to 8-week-old female C57BL/6 mice purchased from Jackson Laboratories (Bar Harbor, ME). These mice were maintained and treated in compliance with NIH guidelines and as approved by the UNC Institutional Animal Care and Use Committee (IACUC). Recombinant AAV vectors packaging a CBh-scGFP transgene or $1 \times$ PBS (as mock treatment) were administered at a dose of 5×10^{11} vg via tail vein injection. Animals were sacrificed 3 weeks postinjection with an intraperitoneal injection of tribromoethanol (Avertin) (0.2 ml of 1.25% solution) followed by transcardial perfusion with 30 ml of $1 \times$ PBS followed by 30 ml of 4% paraformaldehyde in PBS. Tissues were extracted and postfixed for 48 h, and brain and liver tissues were sectioned (generating 50- μ m-thick sections) using a Leica VT 1200S vibrating blade microtome (Leica Biosystems, IL). Brain sections were then immunostained as described below.

Tissue processing and histological analysis. Free-floating, 50- μ m-thick coronal brain sections were stained in 24-well plates. First, sections were blocked with buffer containing 10% goat serum and 1% Triton X (Sigma-Aldrich) in $1 \times$ PBS for 1 h at room temperature. The primary antibody incubation was then performed at 4°C overnight with a primary monoclonal rabbit anti-GFP antibody (1:750) (G10362; Life Technologies) diluted in blocking buffer. The next day, three 10-min washes were performed with $1 \times$ PBS, and subsequent immunostaining was performed using a Vectastain ABC kit (rabbit IgG PK-4001 kit; Vector Biolabs, Burlingame, CA). Immunostained brain sections were finally mounted onto microscopy slides and digitally imaged using bright-field microscopy (20 \times objective) using an Aperio ScanScope XT instrument (Aperio Technologies, Vista, CA) by the University of North Carolina (UNC) Translational Pathology Laboratory. Images were obtained using a Leica eSlide Manager (centralized image storage and data management software) and analyzed using Aperio ImageScope and WebViewer software. Quantifications of cellular transduction were calculated by counting the number of GFP⁺ neuronal or glial cells, determined based upon morphology, per 50- μ m coronal brain section. Data were graphed, and statistical analyses were performed as outlined above. Specific brain regions were identified based upon comparison to a coronal mouse brain reference obtained from the Allen Mouse Brain Atlas. To assay for GFP expression in the liver, sections were stained with the anti-GFP primary antibody as described above; however, an anti-rabbit goat antibody conjugated to Alexa-488 was instead used as the secondary antibody at a dilution of 1:500 (anti-rabbit, ab96883; Abcam). These sections were then imaged with an EVOS FL epifluorescence cell imaging system (AMC/Life Technologies) using a GFP light cube (excitation, 470 nm; emission, 510 nm). Relative fluorescence was quantified from these images using ImageJ software; data were plotted, and statistical analyses were carried out as described earlier, using GraphPad Prism 7 software.

Vector genome biodistribution. Animal studies were performed as described above. DNA was extracted and purified from paraformaldehyde-fixed 50- μ m-thick tissue sections using a QIAamp DNA FFPE Tissue kit (catalog no. 56404; Qiagen). Viral genome copy numbers were then determined for each tissue using quantitative PCR with primers specific to the chicken beta actin (CBA) promoter/cytomegalovirus (CMV) enhancer element sequence driving the CBh-GFP transgene (forward, 5'-TGTTCCCATAGTAACGCCAA-3'; reverse, 5'-TGCCCAAGTAGGAAAGTCCCAT-3'). These viral genome copy numbers were then normalized to the level of the mouse lamin B2 housekeeping gene using specific primers (forward, 5'-GGACCAAGGACTACCTCAAGGG-3'; reverse, 5'-AGGGCACCTCCATCTCGGAAAC-3'). The biodistribution of viral genomes is represented as the ratio of vector genomes per cell recovered for each tissue.

Structural modeling. Amino acid sequences and coordinates for the AAV1 VP3 structure (PDB accession no. 3NG9) were used to generate three-dimensional homology models for the capsid variants (14, 39). SWISS-MODEL (<http://swissmodel.expasy.org/>) was used for structural prediction based on homology to the AAV1 capsid (40, 41). Subsequently, a structure-based alignment was generated using the secondary structure matching (SSM) application in WinCoot software, again using the AAV1 VP3 monomer as a template. The VIPERdb oligomer generator utility (http://viperdbscripps.edu/oligomer_multi.php) was then used to generate oligomeric structural models of the VP3 trimer/3-fold symmetry axes, the VP3 trimer dimers/2-fold symmetry axes, and the full capsid (60-mers) (42). Lastly, PyMOL (Molecular Graphics System, Schrödinger LLC, Cambridge, MA [<http://www.pymol.org/>]) was used to visualize surface-rendered depictions.

Data and statistical analysis. All quantitative data were plotted, and statistical analyses were carried out using GraphPad Prism, version 7, software. One-way analysis of variance (ANOVA) was used to demonstrate statistical significance.

ACKNOWLEDGMENTS

B.H.A. and A.A. designed the overall study, analyzed the data, and wrote the manuscript. B.H.A. executed experiments as well as viral vector production. B.H.A., K.E.S., M.P., and G.W.D. carried out animal studies.

We thank members of the Asokan lab for their support and valued feedback as well as Vicki Madigan for help with statistical analysis.

This study was supported by NIH grants awarded to A.A. (R01HL089221, R01GM122708, R01NS099731, and P01HL112761). We are also grateful to the UNC Translational Pathology Laboratories Core for assisting with slide scanning.

A.A. is a cofounder of StrideBio, LLC, a company focused on commercializing AAV technologies for gene therapy and editing. B.H.A. and A.A. are inventors on patents licensed to StrideBio by UNC-Chapel Hill.

REFERENCES

- Deverman BE, Ravina BM, Bankiewicz KS, Paul SM, Sah D. 2018. Gene therapy for neurological disorders: progress and prospects. *Nat Rev Drug Discov* 17:767. <https://doi.org/10.1038/nrd.2018.158>.
- Murliharan G, Samulski RJ, Asokan A. 2014. Biology of adeno-associated viral vectors in the central nervous system. *Front Mol Neurosci* 7:76. <https://doi.org/10.3389/fnmol.2014.00076>.
- Bedbrook CN, Deverman BE, Gradinaru V. 2018. Viral strategies for targeting the central and peripheral nervous systems. *Annu Rev Neurosci* 41:323–348. <https://doi.org/10.1146/annurev-neuro-080317-062048>.
- Berns K, Parrish CR. 2007. Parvoviridae, p 2437–2477. In Knipe DM, Howley PM, Griffin DE, Lamb RA, Martin MA, Roizman B, Straus SE (ed), *Fields virology*, 5th ed, vol 2. Lippincott Williams & Wilkins, Philadelphia, PA.
- Gao G, Vandenberghe L, Wilson J. 2005. New recombinant serotypes of AAV vectors. *Curr Gene Ther* 5:285–297. <https://doi.org/10.2174/1566523054065057>.
- Kotterman MA, Schaffer DV. 2014. Engineering adeno-associated viruses for clinical gene therapy. *Nat Rev Genet* 15:445–451. <https://doi.org/10.1038/nrg3742>.
- Chapman MS, Agbandje-McKenna M. 2006. Atomic structure of viral particles, p 107–123. In Kerr JR, Cotmore SF, Bloom ME, Linden RM, Parrish CR (ed), *Parvoviruses*. Edward Arnold, Ltd., New York, NY.
- Gurda BL, DiMattia MA, Miller EB, Bennett A, McKenna R, Weichert WS, Nelson CD, Chen WJ, Muzyczka N, Olson NH, Sinkovits RS, Chiorini JA, Zolotukhin S, Kozlyeva OG, Samulski RJ, Baker TS, Parrish CR, Agbandje-McKenna M. 2013. Capsid antibodies to different adeno-associated virus serotypes bind common regions. *J Virol* 87:9111–9124. <https://doi.org/10.1128/JVI.00622-13>.
- Pillay S, Carette JE. 2017. Host determinants of adeno-associated viral vector entry. *Curr Opin Virol* 24:124–131. <https://doi.org/10.1016/j.coviro.2017.06.003>.
- Harbison CE, Chiorini JA, Parrish CR. 2008. The parvovirus capsid odyssey: from the cell surface to the nucleus. *Trends Microbiol* 16: 208–214. <https://doi.org/10.1016/j.tim.2008.01.012>.
- Huang L-Y, Halder S, Agbandje-McKenna M. 2014. Parvovirus glycan interactions. *Curr Opin Virol* 7:108–118. <https://doi.org/10.1016/j.coviro.2014.05.007>.
- Shen S, Horowitz ED, Troupes AN, Brown SM, Pulicherla N, Samulski RJ, Agbandje-McKenna M, Asokan A. 2013. Engraftment of a galactose receptor footprint onto adeno-associated viral capsids improves transduction efficiency. *J Biol Chem* 288:28814–28823. <https://doi.org/10.1074/jbc.M113.482380>.
- Bell CL, Gurda BL, Vliet K, Van Agbandje-McKenna M, Wilson JM. 2012. Identification of the galactose binding domain of the AAV9 capsid. *J Virol* 86:7326–7333. <https://doi.org/10.1128/JVI.00448-12>.
- Huang L-Y, Patel A, Ng R, Miller EB, Halder S, McKenna R, Asokan A, Agbandje-McKenna M. 2016. Characterization of the adeno-associated virus 1 and 6 sialic acid binding site. *J Virol* 90:5219–5230. <https://doi.org/10.1128/JVI.00161-16>.
- Yang B, Li S, Wang H, Guo Y, Gessler DJ, Cao C, Su Q, Kramer J, Zhong L, Ahmed SS, Zhang H, He R, Desrosiers RC, Brown R, Xu Z, Gao G. 2014. Global CNS transduction of adult mice by intravenously delivered rAAVrh.8 and rAAVrh.10 and nonhuman primates by rAAVrh.10. *Mol Ther* 22:1299–1309. <https://doi.org/10.1038/mt.2014.68>.
- Zhang H, Yang B, Mu X, Ahmed SS, Su Q, He R, Wang H, Mueller C, Sena-Estevés M, Brown R, Xu Z, Gao G. 2011. Several rAAV vectors efficiently cross the blood-brain barrier and transduce neurons and astrocytes in the neonatal mouse central nervous system. *Mol Ther* 19:1440–1448. <https://doi.org/10.1038/mt.2011.98>.

17. Albright BH, Storey CM, Murlidharan G, Castellanos Rivera RM, Berry GE, Madigan VJ, Asokan A. 2018. Mapping the structural determinants required for AAVrh.10 transport across the blood-brain barrier. *Mol Ther* 26:510–523. <https://doi.org/10.1016/j.ymthe.2017.10.017>.
18. Wu Z, Miller E, Agbandje-McKenna M, Samulski RJ. 2006. α 2,3 and α 2,6 N-linked sialic acids facilitate efficient binding and transduction by adeno-associated virus types 1 and 6. *J Virol* 80:9093–9103. <https://doi.org/10.1128/JVI.00895-06>.
19. Hahm HS, Broecker F, Kawasaki F, Mietzsch M, Heilbronn R, Fukuda M, Seeberger PH. 2017. Automated glycan assembly of oligo-N-acetylactosamine and keratan sulfate probes to study virus-glycan interactions. *Chem* 2:114–124. <https://doi.org/10.1016/j.chempr.2016.12.004>.
20. Zincarelli C, Soltys S, Rengo G, Rabinowitz JE. 2008. Analysis of AAV serotypes 1–9 mediated gene expression and tropism in mice after systemic injection. *Mol Ther* 16:1073–1080. <https://doi.org/10.1038/mt.2008.76>.
21. Nathwani AC, Cochrane M, McIntosh J, Ng CY, Zhou J, Gray JT, Davidoff AM. 2009. Enhancing transduction of the liver by adeno-associated viral vectors. *Gene Ther* 16:60–69. <https://doi.org/10.1038/gt.2008.137>.
22. Burg M, Rosebrough C, Drouin LM, Bennett A, Mietzsch M, Chipman P, McKenna R, Sousa D, Potter M, Byrne B, Jude Samulski R, Agbandje-McKenna M. 2018. Atomic structure of a rationally engineered gene delivery vector, AAV2.5. *J Struct Biol* 203:236–241. <https://doi.org/10.1016/j.jsb.2018.05.004>.
23. Ng R, Govindasamy L, Gurda BL, McKenna R, Kozyreva OG, Samulski RJ, Parent KN, Baker TS, Agbandje-McKenna M. 2010. Structural characterization of the dual glycan binding adeno-associated virus serotype 6. *J Virol* 84:12945–12957. <https://doi.org/10.1128/JVI.01235-10>.
24. Pillay S, Meyer NL, Puschnik AS, Davulcu O, Diep J, Ishikawa Y, Jae LT, Wosen JE, Nagamine CM, Chapman MS, Carette JE. 2016. An essential receptor for adeno-associated virus infection. *Nature* 530:108–112. <https://doi.org/10.1038/nature16465>.
25. Pillay S, Zou W, Cheng F, Puschnik AS, Meyer NL, Ganaie SS, Deng X, Wosen JE, Davulcu O, Yan Z, Engelhardt JF, Brown KE, Chapman MS, Qiu J, Carette JE. 2017. AAV serotypes have distinctive interactions with domains of the cellular receptor AAVR. *J Virol* 91:e00391–17. <https://doi.org/10.1128/JVI.00391-17>.
26. Wang M, Sun J, Crosby A, Woodard K, Hirsch ML, Samulski RJ, Li C. 2017. Direct interaction of human serum proteins with AAV virions to enhance AAV transduction: immediate impact on clinical applications. *Gene Ther* 24:49–59. <https://doi.org/10.1038/gt.2016.75>.
27. Denard J, Beley C, Kotin R, Lai-Kuen R, Blot S, Leh H, Asokan A, Samulski RJ, Moullier P, Voit T, Garcia L, Svinartchouk F. 2012. Human galectin 3 binding protein interacts with recombinant adeno-associated virus type 6. *J Virol* 86:6620–6631. <https://doi.org/10.1128/JVI.00297-12>.
28. Zhang R, Cao L, Cui M, Sun Z, Hu M, Zhang R, Stuart W, Zhao X, Yang Z, Li X, Sun Y, Li S, Ding W, Lou Z, Rao Z. 11 February 2019. Adeno-associated virus 2 bound to its cellular receptor AAVR. *Nat Microbiol* <https://doi.org/10.1038/s41564-018-0356-7>.
29. Lopez-Bueno A, Rubio MP, Bryant N, McKenna R, Agbandje-McKenna M, Almendral JM. 2006. Host-selected amino acid changes at the sialic acid binding pocket of the parvovirus capsid modulate cell binding affinity and determine virulence. *J Virol* 80:1563–1573. <https://doi.org/10.1128/JVI.80.3.1563-1573.2006>.
30. Nam HJ, Gurda-Whitaker B, Gan WY, Ilaria S, McKenna R, Mehta P, Alvarez RA, Agbandje-McKenna M. 2006. Identification of the sialic acid structures recognized by minute virus of mice and the role of binding affinity in virulence adaptation. *J Biol Chem* 281:25670–25677. <https://doi.org/10.1074/jbc.M604421200>.
31. Lipton HL, Kumar ASM, Hertzler S, Reddi HV. 2006. Differential usage of carbohydrate co-receptors influences cellular tropism of Theiler's murine encephalomyelitis virus infection of the central nervous system. *Glycoconj J* 23:39–49. <https://doi.org/10.1007/s10719-006-5436-x>.
32. Kumar AS, Kallio P, Luo M, Lipton HL. 2003. Amino acid substitutions in VP2 residues contacting sialic acid in low-neurovirulence BeAn virus dramatically reduce viral binding and spread of infection. *J Virol* 77:2709–2716. <https://doi.org/10.1128/JVI.77.4.2709-2716.2003>.
33. Maginnis MS, Nelson CD, Atwood WJ. 2015. JC polyomavirus attachment, entry, and trafficking: unlocking the keys to a fatal infection. *J Neurovirol* 21:601–613. <https://doi.org/10.1007/s13365-014-0272-4>.
34. Barbis DP, Chang SF, Parrish CR. 1992. Mutations adjacent to the dimple of the canine parvovirus capsid structure affect sialic acid binding. *Virology* 191:301–308. [https://doi.org/10.1016/0042-6822\(92\)90192-R](https://doi.org/10.1016/0042-6822(92)90192-R).
35. Organtini LJ, Allison AB, Lukk T, Parrish CR, Hafenstein S. 2015. Global displacement of canine parvovirus by a host-adapted variant: structural comparison between pandemic viruses with distinct host ranges. *J Virol* 89:1909–1912. <https://doi.org/10.1128/JVI.02611-14>.
36. Hafenstein S, Bowman VD, Sun T, Nelson CD, Palermo LM, Chipman PR, Battisti AJ, Parrish CR, Rossmann MG. 2009. Structural comparison of different antibodies interacting with parvovirus capsids. *J Virol* 83:5556–5566. <https://doi.org/10.1128/JVI.02532-08>.
37. Kontou M, Govindasamy L, Nam HJ, Bryant N, Llamas-Saiz AL, Foces-Foces C, Hernando E, Rubio MP, McKenna R, Almendral JM, Agbandje-McKenna M. 2005. Structural determinants of tissue tropism and in vivo pathogenicity for the parvovirus minute virus of mice. *J Virol* 79:10931–10943. <https://doi.org/10.1128/JVI.79.17.10931-10943.2005>.
38. Rubio MP, Lopez-Bueno A, Almendral JM. 2005. Virulent variants emerging in mice infected with the apathogenic prototype strain of the parvovirus minute virus of mice exhibit a capsid with low avidity for a primary receptor. *J Virol* 79:11280–11290. <https://doi.org/10.1128/JVI.79.17.11280-11290.2005>.
39. Miller EB, Gurda-Whitaker B, Govindasamy L, McKenna R, Zolotukhin S, Muzyczka N, Agbandje-McKenna M. 2006. Production, purification and preliminary X-ray crystallographic studies of adeno-associated virus serotype 1. *Acta Crystallogr Sect F Struct Biol Cryst Commun* 62:1271–1274. <https://doi.org/10.1107/S1744309106048184>.
40. Bordoli L, Kiefer F, Arnold K, Benkert P, Battey J, Schwede T. 2009. Protein structure homology modeling using SWISS-MODEL workspace. *Nat Protoc* 4:1–13. <https://doi.org/10.1038/nprot.2008.197>.
41. Arnold K, Bordoli L, Kopp J, Schwede T. 2006. The SWISS-MODEL workspace: a web-based environment for protein structure homology modelling. *Bioinformatics* 22:195–201. <https://doi.org/10.1093/bioinformatics/bti770>.
42. Carrillo-Tripp M, Shepherd CM, Borelli IA, Venkataraman S, Lander G, Natarajan P, Johnson JE, Brooks CL, Reddy VS. 2009. VIPERdb2: an enhanced and web API enabled relational database for structural virology. *Nucleic Acids Res* 37:D436–D442. <https://doi.org/10.1093/nar/gkn840>.